Nonparaxial aberrations in the optical Talbot effect probed by quantum-dot fluorescence tomography

Hyosub Kim, Woojun Lee, Hangyeol Lee, and Jaewook Ahn*
Department of Physics, KAIST, Daejeon 305-701, Korea
(Received 22 January 2015; published 16 March 2015)

The Talbot effect is a near-field phenomenon of a coherent wave transmitted through a grating to form self-images at distances of integer multiples of the so-called Talbot length. However, at long distances, the higher-order diffraction waves fail to converge and spatial walk-off aberration occurs. Here, we describe a scheme for measuring the optical Talbot effect including the spatial walk-off aberration. Our approach utilizes a quantum dot fluorescent film as a tomographic means to probe the Talbot intensity patterns. Since the Talbot effect itself is based on diffraction and interference, measuring it with conventional microscopy systems with a limited acceptance angle might not allow for covering aberrations introduced by walk-off effects. The experiment demonstrates that, by utilizing the fluorescent film as an intermediate step and imaging the fluorescence instead, rather than imaging the intensity patterns directly, higher resolution can be achieved and effects not covered by the numerical aperture of the microscope objectiveused for imaging can be observed.

DOI: 10.1103/PhysRevA.91.033817 PACS number(s): 42.25.Fx, 42.30.Kq, 81.07.Ta

I. INTRODUCTION

First discovered more than a century ago by Talbot [1,2], the near-field diffraction phenomenon of self-image formation, the *Talbot effect*, has been studied in a variety of spectral ranges of electromagnetic waves, extending from infrared, visible, and ultraviolet lights to terahertz frequency waves and x rays [3–5]. Recent studies have further shown the importance of the Talbot effect in novel phenomena involved with matter-waves, plasmons, and even in extreme light conditions such as nonlinear and quantum optical regimes [5–9]. Significant applications of technical importance have been derived from the Talbot effect, including lithography, subwavelength imaging, surface profiling, and atom cooling, to name a few [10–15].

In the Talbot effect, when a coherent beam of radiation transmits through a one-dimensional (1D) or two-dimensional (2D) grating, self-images are formed at distances of multiple integers of the *Talbot length* Z_{Talbot}, and periodically structured subpatterns of images, so-called fractional Talbot carpet patterns, also appear at distances of the fractional multiples of Z_{Talbot}. When we consider an incident wave of a wave vector $k = 2\pi/\lambda$ propagating along the z direction, through a 2D amplitude grating of period d in the x-y plane at $z = 0$, the field amplitude is given by the Fourier propagation method,

$$U(\mathbf{r},z) = \sum_{\mathbf{G}} \tilde{t}(\mathbf{G}) e^{i\mathbf{G}\cdot\mathbf{r}} e^{i(k^2-\mathbf{G}^2)^{1/2}z}, \tag{1}$$

where $\mathbf{r}$ is the vector in the x-y plane, $\tilde{t}(\mathbf{G})$ is the transmission amplitude function of the grating defined in the reciprocal space and $\mathbf{G}$ is the reciprocal lattice vector for the grating. Under the paraxial approximation, which is satisfied by $\gamma \equiv d/\lambda \approx 100$, the propagation field is obtained from the first-order binomial expansion of the propagation phase, i.e.,

$$e^{i(k^2-\mathbf{G}^2)^{1/2}z} \approx e^{ikz} e^{-i\frac{kz}{2}\sin^2\theta_{\mathbf{G}}}, \tag{2}$$

where $\theta_{\mathbf{G}} \equiv \sin^{-1}|\mathbf{G}|/k$ is the angle of each diffraction field propagating along $\mathbf{G}$. When the constructive interference condition, $\exp(-ikz\sin^2\theta_{\mathbf{G}}/2) = 1$, holds for all $\theta_{\mathbf{G}}$, the well-known Talbot length formula is obtained as

$$Z_{\text{Talbot}} = 2d^2/\lambda, \tag{3}$$

for square-lattice gratings [1]. Talbot interference patterns in this regime can be imaged by conventional microscopy with axial scanning [3], and the image resolution is Abbe diffraction limited [16]. At a regime satisfying $\gamma \sim 1$, a new form of the Talbot length formula

$$Z_{\text{Talbot}} = \lambda/(1-\sqrt{1-\lambda^2/d^2}) \tag{4}$$

is available for special cases in $1 < \gamma < \sqrt{2}$ [17]. Instead of such a scalar theory prediction, one can also use numerical vector calculations such as the Fourier modal method (FMM) [18] or the finite-difference time domain (FDTD) calculation [19,20] to obtain the wavelength-scale interference patterns in this regime. High-resolution far-field imaging techniques, such as high numerical aperture microscopy [21–23] and confocal microscopy [17,24], or local-field detection techniques, such as near-field scanning optical microscopy (NSOM), can be used to probe the patterns [12,25]. However, in the *postparaxial approximation* regime, $\gamma \sim 10$, between the above two cases, the Talbot distance formula becomes rather complicated. When the second-order binomial expansion term of $\exp[i(k^2 - \mathbf{G}^2)^{1/2}z]$ is taken into account [7,26], the formula can be formally described in terms of modified Pearcey functions [26,27]. The self-image formation also becomes incomplete, because some of the high-order diffraction waves are either evanescent $|\mathrm{G}| > k$, or limited by the finite lateral size of the grating, $2\tan\theta_{\mathrm{G}} > D/Z_{\text{Talbot}}$, where D denotes the overall size of the grating. Therefore, special microscopic techniques are needed to probe the near-field phenomena in this regime, for example, the leakage radiation microscopy probing plasmonic Talbot effects on metal-dielectric interfaces [28,29].

In this paper, we use a quantum dot (QD) fluorescent film as a tomographic means to study the Talbot effect in the postparaxial approximation regime. The fluorescent

*jwahn@kaist.ac.kr

film is simply inserted and translated in the interference patterns created as a consequence of the Talbot effect, and the QD emission at a different wavelength is captured by a conventional microscope. Since the QD emission does not depend (at least not significantly) on the k spectrum of waves, the intensity maxima of the Talbot carpet in certain near-field regions, not accessible to conventional microscopy systems with a limited numerical aperture, can be measured. In comparison, high-order diffraction waves escape the observation optics, when being measured without the film, causing the spatial walk-off aberration. In the rest of the paper, we first theoretically consider the spatial walk-off aberration and the working principle of the QD-film fluorescence tomography in Sec. II and describe the experimental details in Sec. III. We then present the experimental results including the spatial walk-off effect and the advantage of the QD-film tomography in Sec. IV, before concluding in Sec. V.

II. THEORETICAL CONSIDERATION

The degradation of the Talbot carpet self-image formation of a finite-size grating can be understood as follows. When the propagation distance z is comparable to the total lateral size D of the square-lattice grating, power dissipation through *spatial walk-off* of diffracted waves occurs. As illustrated by simple ray-tracing in Fig. 1(a), each diffraction wave of a distinct diffraction order starts to spatially walk-off from the wave propagation center at the distance $Z_{\text{walk-off}}$ defined by

$$Z_{\text{walk-off}}(\mathbf{G}) = \frac{D}{2\tan\theta_{\mathbf{G}}}. \tag{5}$$

The self-image formation in the Talbot effect thus starts to degrade when the propagation distance z exceeds $Z_{\text{walk-off}}(\mathbf{G}_{\max})$, where $\mathbf{G}_{\max}(\equiv 2\pi n_{\max}/d)$ is the largest available lattice vector, satisfying $n_{\max} < \gamma$ in the case of a square-lattice grating. It is gradually degraded more as z exceeds $Z_{\text{walk-off}}(\mathbf{G})$ of smaller $\mathbf{G}$'s. The walk-off distance is represented in terms of m and n by

$$Z_{m,n} = \frac{D}{2\sqrt{n^2+m^2}}\sqrt{\gamma^2-n^2-m^2}, \tag{6}$$

where (m,n) are integers denoting the indices of each diffraction order, i.e., $\mathbf{G} = \frac{2\pi}{d}(n,m)$.

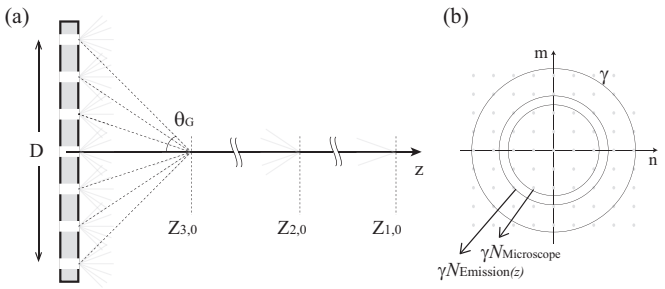

FIG. 1. (a) Schematic drawing of propagating diffraction fields from a grating, with walk-off distances $Z_{n,m}$ illustrated. (b) Diffraction orders are restricted in the reciprocal plane by either the size of the grating $\gamma N_{\text{Emission}}(z)$ or the numerical aperture of the objective lens $\gamma N_{\text{Microscope}}$.

The field intensity averaged over one unit cell in the real domain is given at z by

$$I(z) \equiv \frac{1}{d^2}\iint_{d^2} |U(\mathbf{r},z)|^2 dx dy = \sum_C |\tilde{t}_{n,m}|^2, \tag{7}$$

where $\tilde{t}_{n,m}$ is the transmission amplitude and the summation restriction C is determined by the effective numerical aperture $N_{\text{Emission}}(z) \equiv D/\sqrt{D^2+4z^2}$ of the grating, or

$$C : \sqrt{n^2+m^2} < \frac{\gamma D}{\sqrt{D^2+4z^2}} = \gamma N_{\text{Emission}}(z). \tag{8}$$

Averaging over a period cancels out cross terms, effectively decoupling each diffraction order. When $n_{\max}$ is smaller than $\gamma N_{\text{Emission}}(z)$, a condition that occurs at the position $z < d(\gamma^2 - n_{\max}^2)^{1/2}$, the restriction C is lifted off and all diffraction orders contribute to the interference. However, the numerical aperture of the microscope objective also restricts the collection of the diffraction orders. For a microscope objective located at $z+f$, where f is the working distance of the lens, those diffracted waves of larger diffraction angles than the collection angle of the lens are excluded; thus only those diffraction waves satisfying $\theta_{\text{G}} < \sin^{-1} N_{\text{Microscope}}$ are collected, where $N_{\text{Microscope}}$ denotes the numerical aperture of the microscope objective. Therefore, the summation restriction C is more generally given by

$$C' : \sqrt{n^2+m^2} < \gamma \min(N_{\text{Emission}}(z), N_{\text{Microscope}}). \tag{9}$$

If we define Z_{M}, which we call the microscope distance, in such a way that satisfies $N_{\text{Emission}}(Z_{\text{M}}) = N_{\text{Microscope}}$, the wave collection by the objective lens is limited for $z < Z_{\text{M}}$ by the numerical aperture of the microscope objective, and for $z > Z_{\text{M}}$ by the spatial walk-off effect [see Fig. 1(b)].

However, if we place a fluorescent film at z, the fluorophores absorb all of the diffraction orders allowed by C and emit light in every direction. As it is not limited by C', the numerical aperture of the objective lens is not restrictive. Thus the intensity even at $z < Z_{\text{M}}$ is governed again by the walk-off effect. Therefore, the use of fluorophores as a tomographic method allows probing of the walk-off effect in $z < Z_{\text{M}}$, which is not available for a conventional microscope.

III. EXPERIMENT

The experimental setup is schematically shown in Fig. 2. To image the 2D sections of the Talbot carpet, a QD film was placed at a distance fixed from the microscope objective. The grating, instead of the QD film or the lens, was longitudinally translated for the propagation distance z. We performed three experiments: (1) the Talbot carpet imaging using the proposed method, (2) the spatial walk-off aberration effect, and (3) the advantage of the QD-film tomography over conventional microscopy. For these, we used two types of light sources, a 406-nm light from a frequency-doubled Ti:sapphire-pulsed laser for the QD (the first and third) experiments and a 532-nm light from a diode-pumped solid state (Nd:YAG) cw laser for the second. For the 406-nm laser pulses, we initially generated 30-fs-short infrared (IR) laser pulses wavelength-centered at 812 nm from a Ti:sapphire mode-locked laser oscillator operating at a repetition rate of 80 MHz, and then frequency

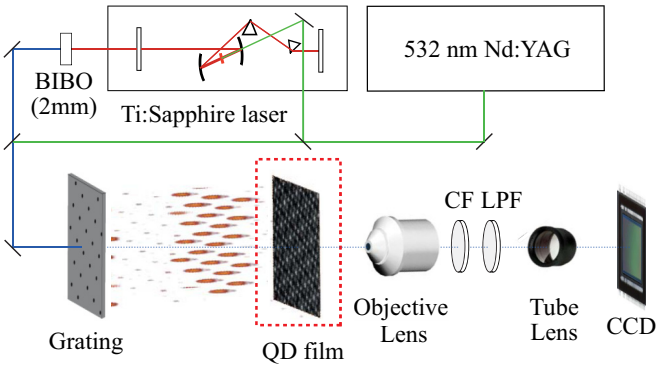

FIG. 2. (Color online) Schematic experimental setup for QD-film fluorescence tomography. The light source was either narrow-band 532-nm light or broadband light from a mode-locked laser, depending on the experiment. CF and LPF are acronyms for color filter and long-pass interference filter, respectively.

doubled the IR pulses by a 2-mm-thick BiB_3O_6 (BIBO) crystal to produce 406-nm pulses with a 2-nm bandwidth. The output laser power of 406-nm light was adjusted up to 60 mW and the 2-mm beam diameter ensured homogeneous illumination onto the grating over the area of $250 \times 250\ \mu m^2$.

The 2D amplitude grating mask was fabricated with a periodic array of circular holes with a nominal diameter of 1 μm perforated on a 100-nm-thick chrome film deposited on top of a 5-in fused silica substrate of 2.3-mm thickness. The hole period, or the lattice constant, was $d = 5\ \mu m$ and the number of holes was 50×50. The QD film was made with a CdSe/ZnS core/shell QD solution (Evident Tech. ED-C11-TOL-0520) spin coated on a glass cover-slip of size $24 \times 50 \times 0.17\ mm^3$, to absorb shorter wavelength photons than 513 nm and to emit 526-nm photons. The surface morphology of the fabricated QD film was optically flat when examined with an atomic force microscope. We used three different objective lenses, one for each of the experiments: NA = 1.3 was used in the first experiment to confirm the quality of the QD film, NA = 0.7 in the second experiment for the spatial walk-off aberration, and NA = 0.25 in the third experiment to acquire clear evidence of the advantage of QD-film tomography.

For the detection of the fluorescence from the QD film, we used a color filter and a long-pass interference filter located at the collimated region, as shown in Fig. 2. The relative transmittance in the 400–500-nm spectral region was reduced below 10^{-7}. The interference filter was highly reflective and the 400-nm light was refocused back onto the QD film, causing extra artifact images. To avoid this, we simultaneously used a slightly absorptive color filter. A 200-mm focal length tube lens was used to capture images onto an 8-bit 1240×1064 pixel charged-coupled device (CCD).

IV. RESULTS AND DISCUSSION

Figure 3 shows the three-dimensional (3D) structure of the Talbot carpet interference pattern, imaged by the proposed QD-film fluorescence tomography. The xz-plane image of the measured 3D Talbot carpet is shown in Fig. 3(a) and the xy-plane sectioned images at various distances are shown in

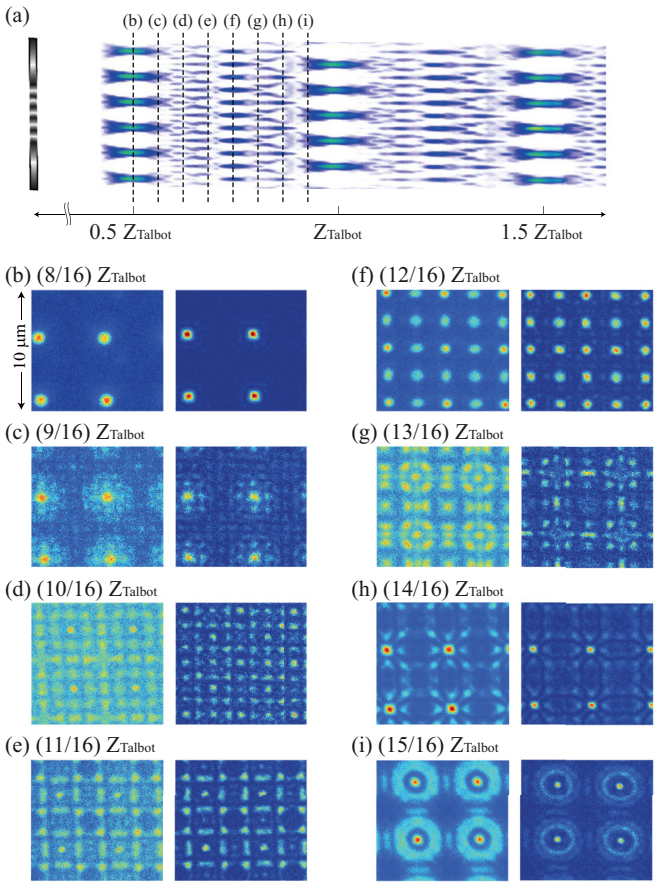

FIG. 3. (Color online) (a) The 3D Talbot carpet imaged by QD-film fluorescence tomography. (b)–(i) Cross-sectional images of the Talbot carpet at various distances ranging from $(8/16)\ Z_{Talbot}$ to $(15/16)\ Z_{Talbot}$. In each figure, the right panel is the result of the FDTD calculation and the left is the tomogram of the QD-film fluorescence tomography.

Figs. 3(b)–3(i). In each figure, the right panel is the computer simulation based on the FDTD calculation, and the left panel is the tomogram of the QD-film fluorescence tomography. The Talbot length measured from the peak-to-peak distance is 119 μm, which is 3% off from $2d^2/\lambda$ =123 μm calculated with the paraxial approximation formula. The measurement agrees well with the result of the postparaxial approximation [26] for $\gamma = 12.3$. The QD-film cross-section images in the left panels show background noise, which is due to the long exposure time of the CCD.

In an ultrafast laser implementation of Talbot interference imaging, the effects of coherence length and chromatic aberration need to be taken into account [30]. The optical path length difference between two different diffraction orders $\mathbf{G}$ and $\mathbf{G}'$ is given by $z/(\cos^{-1}\theta_G - \cos^{-1}\theta'_G)$, which is, for example, 8.5 μm at $z = 600\ \mu m$ for the zeroth and second orders. However, the coherence length of our laser pulse was estimated as 54 μm, long enough for the tested range of the axial distance, $z < 1$ mm. Meanwhile, the Talbot length dispersion $\Delta Z_{Talbot}/Z_{Talbot} = \Delta\lambda/\lambda$ caused by the 2-nm spectral bandwidth of the laser was less than 0.01, much smaller than the postparaxial shift (0.03) of the Talbot length. Therefore the chromatic aberration was sufficiently suppressed

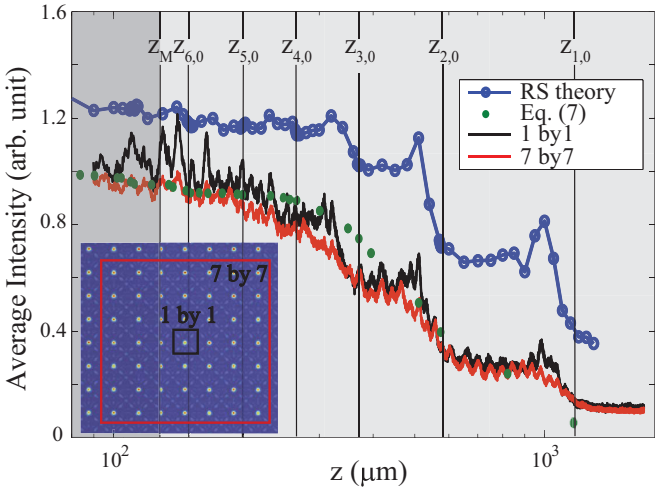

FIG. 4. (Color online) Spatial walk-off effect in Talbot diffraction patterns. Black (dark) and red (light) lines represent the experimental data, averaged intensities over one-by-one and seven-by-seven cells in the real domain (inset), respectively. Green dots denote Eq. (7) and blue dots (with a line through them) the Rayleigh-Sommerfeld diffraction integral, vertically shifted for clarity. Each vertical line corresponds to the walk-off distance $Z_{m,0}$, and the gray area denotes $z < Z_{\mathrm{M}}$. The inset shows the averaging area for each data.

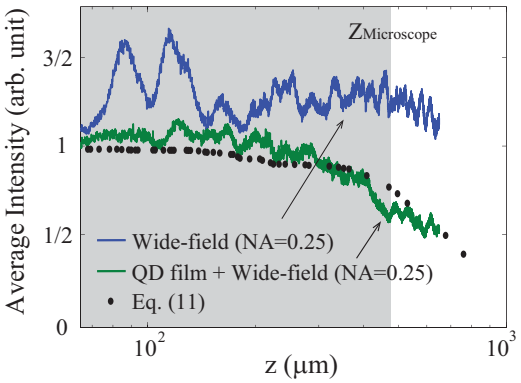

FIG. 5. (Color online) Talbot carpet intensities measured along the axial direction using an NA = 0.25 objective lens and averaged over one lattice period for wide-field microscopy shown in blue and for QD-film tomography in green. Theoretical guide in black dots is shown for comparison. The wide-field microscope data are vertically shifted for clarity.

and the optical path length difference was overcome by the long coherence length.

In the second experiment, we examined the spatial walk-off effect. Figure 4 shows the measured average intensity in Eq. (7) of the Talbot carpet along the axial direction. The intensity curves show clear plateaus in the distance intervals between the walk-off distances, $Z_{1,0} - Z_{2,0}$, $Z_{2,0} - Z_{3,0}$, $Z_{3,0} - Z_{4,0}$, etc. The gray area denotes $z < Z_{\mathrm{M}}$ for $N_{\mathrm{Microscope}} = 0.7$. The experimental result agrees well with the theoretical calculations. The green dots are from Eq. (7) with the summation restriction in Eq. (9), where the lowest dot is from the (1,0) diffraction order, the second lowest is from the (1,0) and (1,1) orders, and so on. The blue dots (with a line through them) are based on the scalar Rayleigh-Sommerfeld (RS) diffraction integral over one primitive cell [31]. The black (dark) line, the averaged experimental result over one primitive cell, shows steplike degradation, which fits well with the RS diffraction integral. Both the experiment and calculation show that the diffraction order $(m,0)$ makes a greater contribution than the order (m,n) for $n \neq 0$. This behavior can be easily understood because the effective walk-off distances of $n \neq 0$ diffractions are in fact bigger than those defined in Eq. (6). For example, the lateral size of the square-lattice grating is smallest along the x and y directions and greatest along their diagonal direction, along which the effective grating size is $D' = \sqrt{2}D$. However, the red (light) line, averaged over seven-by-seven cells, and the green dots from Eq. (7) show smooth intensity change, which is attributable to the finite-size of the grating causing apodization. Note that the result in Eq. (7) not only neglects the variation in D but is also derived under the assumption of the discontinuities at the wave front boundaries. Nevertheless, the result in Eq. (7) shows a decent agreement with experiments.

Lastly, we performed a proof-of-principle demonstration of the advantage of QD-film fluorescence tomography over conventional wide-field microscopy. For this, we used an objective lens of a low numerical aperture, NA = 0.25. The light source was the $\lambda = 406$ nm pulse, and the QD emitted at $\lambda' = 526$ nm. Experimental data of the averaged intensities along the axial z direction with and without the QD film are, respectively, shown in Fig. 5. The result of the conventional wide-field microscopy, represented in blue, shows distinctly different behavior from that of the QD-film fluorescence tomography in green (vertically shifted for clarity). In the gray area (for $z < Z_{\mathrm{microscope}}$) in Fig. 5, the blue line (wide-field microscopy) is roughly flat, because the collected light is limited by $N_{\mathrm{Microscope}}$. However, the green line (QD-film tomography) exhibits the spatial walk-off effect, an increase in the average intensity as z approaches zero. The result of the QD-film tomography (green line) shows a good agreement with the theoretical result (black dots) from Eq. (7). The result indicates that the QD-film tomography collects diffraction information of the Talbot carpet, information that is otherwise missing in conventional wide-field microscopy. The proposed method, therefore, suggests a practical approach to acquiring a large field-of-view without losing information in the far-field regime by paying-off lateral resolution.

V. CONCLUSION

In summary, we have considered the spatial walk-off aberration of the postparaxial Talbot effect. The experiment carried out by the QD-film fluorescence tomography has demonstrated that the high-order diffraction waves that exceed the acceptance angle of conventional microscopes can be successfully captured to reconstruct the 3D intensity profile of the optical Talbot carpet. The simple reason for this behavior is the fact that the QD emission does not depend (at least not significantly) on the k spectrum of waves creating intensity maxima (exciting the QDs) in the Talbot images. Therefore, the "real" intensity maps can be measured (given the fact that the QDs in the film have equal efficiencies) without being limited by the observation optics. In contrast, the observed intensities without the film would depend on the angular

spread of the waves creating the intensity features, because the observation optics have a limited acceptance angle. The Rayleigh-Sommerfeld diffraction calculation performed in the postparaxial approximation regime shows good agreement with the experimental result. It is hoped that this method, in conjunction with multiphoton excitation, will be useful for subwavelength axial and lateral resolution microscopy.

ACKNOWLEDGMENTS

We greatly acknowledge generous assistance and valuable information on quantum dots provided by H. C. Park, Prof. Y. H. Cho, and Dr. S. Jeong. We also thank the anonymous referee for valuable comments. This research was supported by Samsung Science and Technology Foundation [SSTF-BA1301-12].

[1] H. F. Talbot, Philos. Mag. **9**, 401 (1836).
[2] F. R. S. Rayleigh, Philos. Mag. **11**, 196 (1881).
[3] W. B. Case, M. Tomandl, S. Deachapunya, and M. Arndt, Opt. Express **17**, 20966 (2009).
[4] F. Pfeiffer, T. Weitkamp, O. Bunk, and C. David, Nat. Phys. **2**, 258 (2006).
[5] J. Wen, Y. Zhang, and M. Xiao, Adv. Opt. Photonics **5**, 83 (2013).
[6] L. Deng, E. W. Hagley, J. Denschlag, J. E. Simsarian, Mark Edwards, Charles W. Clark, K. Helmerson, S. L. Rolston, and W. D. Phillips, Phys. Rev. Lett. **83**, 5407 (1999).
[7] M. R. Dennis, N. I. Zheludev, and F. J. Garcia de Abajo, Opt. Express **15**, 9692 (2007).
[8] Y. Zhang, J. Wen, S. N. Zhu, and M. Xiao, Phys. Rev. Lett. **104**, 183901 (2010).
[9] M. Berry, I. Marzoli, and W. Schleich, Phys. World 39 (2001).
[10] A. Isoyan, F. Jiang, Y. C. Cheng, F. Cerrina, P. Wachulak, L. Urbanski, J. Rocca, C. Menoni, and M. Marconi, J. Vac. Sci. Technol. B **27**, 2931 (2009).
[11] L. Stuerzebecher, T. Harzendorf, U. Vogler, U. D. Zeitner, and R. Voelkel, Opt. Express **18**, 19485 (2010).
[12] F. M. Huang, N. Zheludev, Y. Chen, and F. J. G. de Abajo, Appl. Phys. Lett. **90**, 091119 (2007).
[13] O. Bryngdahl, J. Opt. Soc. Am. **63**, 416 (1973).
[14] M. Thakur, C. J. Tay, and C. Quan, Appl. Opt. **44**, 2541 (2005).
[15] C. Mennerat-Robilliard, D. Boiron, J. M. Fournier, A. Aradian, P. Horak, and G. Grynberg, Europhys. Lett. **44**, 442 (1998).
[16] E. Abbe, J. R. Microsc. Soc. **1**, 388 (1881).
[17] Y. Hua, J. Y. Suh, W. Zhou, M. D. Huntington, and T. W. Odom, Opt. Express **20**, 14284 (2012).
[18] L. Li, J. Opt. Soc. Am. A **14**, 2758 (1997).
[19] S. Teng, X. Chen, T. Zhou, and C. Cheng, J. Opt. Soc. Am. A **24**, 1656 (2007).
[20] S. Teng, Y. Tan, and C. Cheng, J. Opt. Soc. Am. A **25**, 2945 (2008).
[21] M. S. Kim, T. Scharf, C. Menzel, C. Rockstuhl, and H. P. Herzig, Opt. Express **20**, 4903 (2012).
[22] M. S. Kim, T. Scharf, C. Menzel, C. Rockstuhl, and H. P. Herzig, Opt. Express **21**, 1287 (2013).
[23] Y. Yu, D. Chassaing, T. Scherer, B. Landenberger, and H. Zappe, Plasmonics **8**, 723 (2013).
[24] H. Gao, J. K. Hyun, M. H. Lee, J.-C. Yang, L. J. Lauhon, and T. W. Odom, Nano Lett. **10**, 4111 (2010).
[25] A. Nesci, R. Dändliker, G. Salt, and H. P. Herzig, Opt. Commun. **205**, 229 (2002).
[26] J. D. Ring, J. Lindberg, C. J. Howls, and M. R. Dennis, J. Opt. **14**, 075702 (2012).
[27] T. Pearcey, Philos. Mag. **37**, 311 (1946).
[28] W. Zhang, C. Zhao, J. Wang, and J. Zhang, Opt. Express **17**, 19757 (2009).
[29] A. Drezet, A. Hohenau, A. L. Stepanov, H. Ditlbacher, B. Steinberger, N. Galler, F. R. Aussenegg, A. Leitner, and J. R. Krenn, Appl. Phys. Lett. **89**, 091117 (2006).
[30] G. Mínguez-Vega, Y. O. Mendoza, M. Fernández Alonso, P. Andrées, V. Climent Jordá, and J. Lancis Sáez, Opt. Commun. **281**, 374 (2008).
[31] A. Dubra and J. A. Ferrari, Am. J. Phys. **67**, 87 (1999).